Structural coupling mechanism of high strength steel and mild steel under multiaxial cyclic loading

Fatemeh Javidan [*1], Amin Heidarpour [1a], Xiao-Ling Zhao [1b] and Riadh Al-Mahaidi [2b]

[1] *Department of Civil Engineering, Monash University, Melbourne, Australia*
[2] *Department of Civil and Construction Engineering, Swinburne University of Technology, Melbourne, Australia*

Abstract. High strength steel is widely used in industrial applications to improve the load-bearing capacity and reduce the overall weight and cost. To take advantage of the benefits of this type of steel in construction, an innovative hybrid fabricated member consisting of high strength steel tubes welded to mild steel plates has recently been developed. Component-scale uniaxial and multiaxial cyclic experiments have been conducted with simultaneous constant or varying axial compression loads using a multi-axial substructure testing facility. The structural interaction of high strength steel tubes with mild steel plates is investigated in terms of member capacity, strength and stiffness deterioration and the development of plastic hinges. The deterioration parameters of hybrid specimens are calibrated and compared against those of conventional steel specimens. Effect of varying axial force and loading direction on the hysteretic deterioration model, failure modes and axial shortening is also studied. Plate and tube elements in hybrid members interact such that the high strength steel is kept within its ultimate strain range to prevent sudden fracture due to its low ultimate to yield strain ratio while the ductile performance of plate governs the global failure mechanism. High strength material also significantly reduces the axial shortening in columns which prevents undesirable frame deformations.

Keywords: high strength steel tubes; hybrid fabricated members; lateral cyclic loading; varying axial force, hysteretic deterioration, ductile failure

1. Introduction

Apart from the increase in load-bearing capacity, one of the main benefits of incorporating high strength steel material in a structure is the significant reduction in the overall weight. For structures designed for seismic-prone areas, reducing the overall system mass leads to the reduction of distributed shear force at different levels which can be achieved by utilizing high strength materials. In addition to the structural and mechanical advantages, the incorporation of high strength steel components reduces transportation and construction costs due to its similar density to mild steel. To improve the performance of high strength structural elements, innovative hybrid sections are proposed which are fabricated from tubes of high grade steel welded to the corners of mild steel plates, forming a high performance hollow steel section. The performance of these sections has been studied under various loading cases such as monotonic compression, bending and fire (Ye *et al.* 2007, Heidarpour *et al.* 2014, Javidan *et al.* 2016a, 2017, Farahi *et al.* 2017). Monotonic compression tests conducted on the component-scale fabricated steel members showed an increase of up to three times in strength compared to

conventional welded box sections (Javidan *et al.* 2016a) and cold-formed hollow steel sections (Javidan *et al.* 2015b) with equivalent cross-sectional areas and weights. It was found from these studies that the structural plate-tube interaction in these sections results in a reasonable increase in the ductility of structural components compared to what is expected from the high strength steel material alone.

Although the monotonic performance of the proposed structural members under quasi-static loading has been investigated, the seismic behavior of these elements still remains unknown. The closed hollow geometry of these hybrid sections makes them less vulnerable to lateral torsional instabilities compared to deep steel sections, especially in tall moment-resisting frames subjected to combined axial and cyclic lateral loading Fogarty and El-Tawil 2016). As opposed to the wide range of studies available on the cyclic performance of hollow steel sections (Aoki and Susantha 2005, Nakashima and Liu 2005, Park *et al.* 2012, Amadio *et al.* 2017, Farahi and Erfani 2017) consisting of mild steel material, limited research is available on the cyclic performance of high strength steel structural elements, most of which involve steel grades up to 700 MPa. Experimental and numerical investigations were conducted on H-shaped and box sections with steel yield strengths of 460 and 700MPa under cyclic loading (Wang *et al.* 2014, 2015). Hollow structural steel sections with a yield strength around 400MPa were considered under cyclic bending to study the influence of geometry on yielding and plastic hinging behavior (Fadden and

---

*Corresponding author, Ph.D.,
  E-mail: fatemeh.javidan@monash.edu
[a] Ph.D., Senior Lecturer
[b] Professor

McCormick 2012). Building frames consisting of column elements with high strength steel material (up to grade 700) were proposed and studied to improve the seismic resistance (Dubina *et al*. 2014). A dual phase eccentrically braced frame consisting of conventional steel links and high strength steel beams, columns and braces showed reliable hysteretic behavior and reduced material costs (Lian *et al*. 2015).

To understand the lateral bending and cyclic load-bearing performance of fabricated hybrid sections, basic deformation-controlled unidirectional cyclic tests are performed considering the effect of axial gravity forces. Many experimental and numerical studies on hollow thin-walled steel beam-columns under cyclic bidirectional loading confirm the considerable effect of additional cyclic loading direction on the seismic mechanical performance of steel members, such as strength and ductility (Goto *et al*. 2006, Kulkarni *et al*. 2009, Mamaghani 2010, Ucak and Tsopelas 2015). In these studies, various bidirectional loading patterns with circular and square load paths were applied along with simultaneous axial loads at a specific ratio of the axial capacity. Furthermore, the vertical component of earthquake leads to varying applied axial load, affecting column degradation (Rodrigues *et al*. 2016). This can be practically modelled by applying varying axial loads proportional to lateral seismic excitation. Considering the effect of varying axial forces as lateral amplitudes are applied in one or two directions results in an increase of hysteretic energy dissipation (Bousias *et al*. 1995). Previous investigations, mostly on reinforced concrete specimens, have shown that axial load variations as well as bi-lateral displacements have significant effects on capacity degradation and the nonlinear performance of structural elements. These effects include reductions in the amount of lateral drift corresponding to damage initiation and stiffness degradation (ElMandooh Galal and Ghobarah 2003, Rodrigues *et al*. 2016).

Research on steel sections with yield strength values above 700 MPa is very limited (Banfi *et al*. 2005, Girão
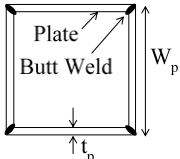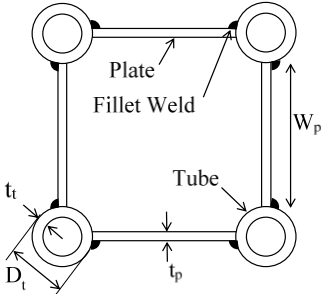
Coelho and Bijlaard 2010, Amraei *et al*. 2016), l*et al*one under lateral and axial cyclic loadings. Following the previous series of experimental tests conducted on the hybrid sections, this paper focuses on the behavior of these sections under multiaxial cyclic loads. In order to quantify the hysteretic performance of fabricated hybrid sections, uniaxial cyclic tests have been conducted under unilateral displacement-controlled conditions with constant axial forces. Furthermore, multiaxial cyclic tests have been performed investigating the coupled influence of varying axial forces and bilateral cyclic deformations. Strength and stiffness degradations are compared considering the effect of steel tube material. Plastic hinge development along hybrid members is also studied in the case of unilateral and bilateral reversed amplitudes. Influence of tube material, loading directions and varying compression force on failure modes and axial shortening of sections are also described. Results of the complete set of experimental cyclic tests and calibration of model parameters leads to an overview of the seismic performance of thin-walled high strength fabricated hybrid sections to accurately assess structures consisting of these types of high capacity components from the onset of damage through to collapse. This study has been conducted as part of a group research study on steel and fabricated hybrid elements under extreme loading scenarios (Mirmomeni *et al*. 2015, Nassirnia *et al*. 2015, Hosseini *et al*. 2016, Sinaie *et al*. 2016, Azhari *et al*. 2017, Sadeghi *et al*. 2017).

2. Design of experiments

2.1 Test plan

The hybrid fabricated specimens considered in this paper are square-shaped hollow sections consisting of mild steel plates with circular tubes welded to the corners. The cross section and dimensions of these hollow steel members are shown in the first column of Table 1. The geometry and

Table 1 Description of specimen specifications and testing conditions

Specimen geometry (Dimensions units: mm)		Test label	Material	Nominal length	Loading conditions	
					Lateral	Axial
	$W_p=340$, $t_p=4$	Box-M	Mild steel plate	2m	Lateral monotonic	Constant
		MS-C-1D	Mild steel plate, Mild steel tube	2m	Unilateral cyclic	Constant
	$D_t=76.1$, $t_t=3.2$, $W_p=210$, $t_p=3$	HSS-C-1D	Mild steel plate, Mild steel tube	2m	Unilateral cyclic	Constant
		UHSS-C-1D	Mild steel plate, HSS tube	2m	Unilateral cyclic	Constant
		UHSS-C-2D	Mild steel plate, UHSS tube	2m	Bilateral cyclic	Varying

material properties considered in the present study are consistent with previous studies conducted on the proposed hybrid sections (Javidan *et al*. 2015a, 2016a, 2017). Due to the lack of design recommendations in current seismic and design standards for the high strength materials, the structural results obtained in previous experiments, such as the compressive strength of hybrid sections, are considered. The mechanical properties of plate and tube steel elements were obtained from standard material testing. Mild steel (MS) tube with yield and ultimate strengths of 305 and 340 MPa, high strength steel (HSS) with yield and ultimate strengths of 770 and 850 MPa and ultra-high strength steel (UHSS) with yield and ultimate strengths of 1250 and 1385 MPa were used. Mild-steel plate elements in all sections have a yield strength and ultimate strength of 265 and 375 MPa, respectively. Tube specimens were externally welded to the corners of plates using gas tungsten arc welding (GTAW). More information regarding the mechanical properties of steel materials, welding and fabrication procedures can be found in previous literature (Javidan *et al*. 2016b). To compare the performance of these fabricated sections with conventional structural sections, a control test was conducted on an equivalent fabricated MS box section with a similar section width and cross-sectional area and therefore similar weight. A monotonic lateral displacement-controlled pushover test was conducted to obtain the lateral backbone curve of this box section for comparison purposes. Table 1 summarizes a description of the characteristics of each section and the relevant test types.

Test labels are presented in the second column of Table 1 representing specimen types throughout the paper. Except for the fabricated box section, the first term of each test label represents the material of the corner tube used in that section. The second term indicates the test type, where M and C stand for monotonic and cyclic, respectively. The third term shows the direction(s) of applied lateral cyclic loading. Three types of fabricated steel specimens (MS-C-1D, HSS-C-1D, UHSS-C-1D) were tested under lateral displacement-controlled cyclic loading in one direction. An additional cyclic test was conducted on a specimen consisting of UHSS tubes (UHSS-C-2D), where lateral displacement was applied cyclically in two directions and the axial load varied as a function of lateral displacement. Displacement-controlled amplitudes were applied based on the testing protocol proposed in FEMA461 (FEMA461 2007). The smallest targeted deformation was chosen such that the predicted lowest damage state would occur after at least six cycles. The amplitude of each step (a_{i+1}) was increased as a function of the previous step's amplitude (a_i) and each cyclic amplitude was repeated twice during testing such that

$$a_{i+1} = 1.4a_i \tag{1}$$

All lateral cyclic displacements were continued until the physical limits of testing machine were reached and major damage in the specimens occurred, which satisfies the minimum total number of cycles (20 cycles) and the
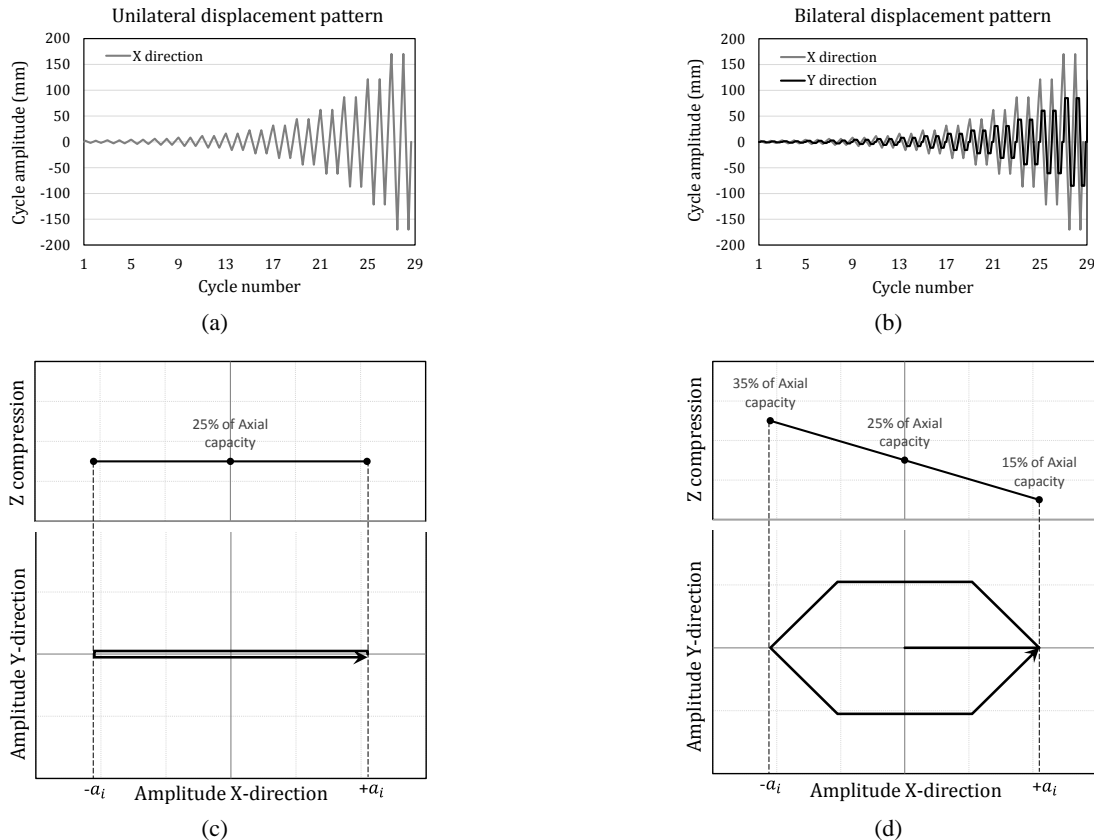

Fig. 1 Deformation controlled loading history: (a) Unilateral test displacement pattern; (b) Bilateral test displacement pattern; (c) Axial force variation in unilateral test for each cycle; (d) Axial force variation in bilateral test for each cycle

magnitude of targeted maximum deformation (story drift: 0.03) recommended by FEMA461. The applied displacement rate was kept within the quasi-static range. All unilateral and bilateral cyclic tests followed a similar displacement history in the lateral X direction, while half of that was applied in the perpendicular Y direction, if applicable. Illustrations of displacement histories are presented in Fig. 1. The applied axial force on each test specimen in MS-C-1D, HSS-C-1D, UHSS-C-1D tests was 25% of the axial capacity of that member obtained from previous studies (Javidan *et al.* 2015b, 2016a). In the multiaxial cyclic test (UHSS-C-2D), axial force varied depending on the lateral amplitude. At zero X direction displacement, specimen was subjected to the mean axial force value, i.e., 25% of the compressive strength of member, in Z direction.

2.2 Testing equipment

Displacement-controlled cyclic tests were performed using the Multi-Axis Substructure Testing (MAST) system (Hashemi *et al.* 2014) which can accommodate the loading capacity and stroke requirements of the intended

test plan. Using the servo-hydraulic control system of MAST, rotation degrees of freedom at both ends were kept zero throughout all tests while end force and moment reactions were measured and recorded. To ensure adequate clamp conditions at both ends, specimen ends were welded to anchor plates and triangular stiffeners were also used at

four sides. In order to meet the testing machine's dimension requirements, two concrete pedestals were used, connecting the top end of column to the MAST crosshead and the bottom end of column to the strong floor. To ensure that no rotation or slip has occurred in the setup during each test, linear variable differential transformers (LVDTs) were set at contact locations to measure and control relative displacements such as relative horizontal displacement measurements for any slip and vertical displacement measurements for any uplifting of the anchor plate. Fig. 2(a) shows various parts of the experimental test setup. It is worth noting that the total effective length of column is obtained from the net span of member, excluding the length of stiffeners at both ends.

2.3 Data acquisition

The main force and displacement measurements of all cyclic tests were obtained from the MAST system actuators.

The acquisition setting of MAST was arranged such that the system motions and forces were controlled and calculated for a coordinate at the center of the column's top surface (see Fig. 2(a)). Apart from the data readings directly obtained from the MAST system, additional displacement and strain measurements were also performed. For displacement and curvature measurements, string pots were attached at three points along the height of each member on one side for unilateral tests and on two sides for the bilateral test. A three-dimensional digital image correlation system
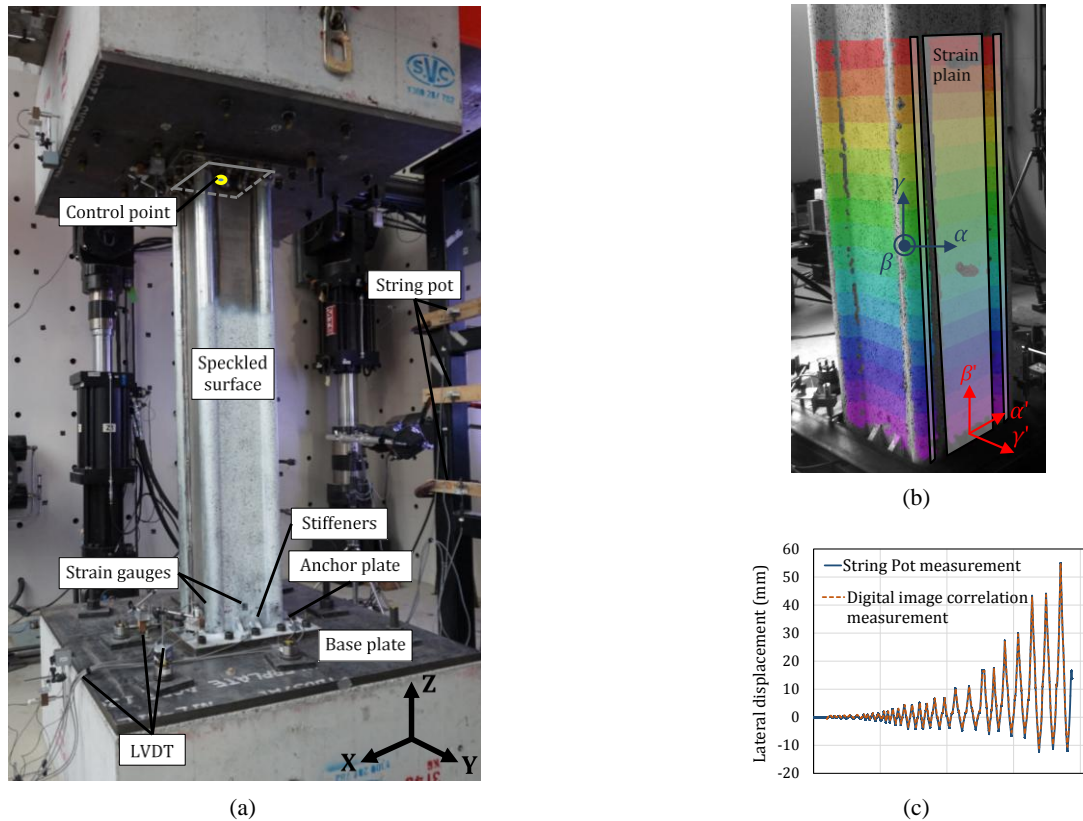

(a)

(b)

(c)

Fig. 2 (a) Multiaxial cyclic experimental setup and global loading coordinates; (b) Digital image correlation system together with local displacement and strain coordinates; (c) Digital image correlation measurement versus string pot reading for an example point

(VIC-3D) was also utilized for non-contact deformation measurements of two perpendicular faces of the bottom half of each specimen. The initial general displacement matrix was transformed to obtain deformations at local column coordinates. Fig. 2(b) shows an example of digital image correlation surface measurement with initial (α, β, γ) and transformed (α', β', γ') coordinate systems. In addition to displacements, strain values were derived from measured displacements at any given 2-D plane. Depending on the column surface from which strain data were intended to be obtained, the deformation matrix was transformed such that the considered surface ended up parallel to the strain plane. Due to the special geometry of members considered in this study, for each side of the column, the derived strain system is applicable to the entire plate surface parallel to the strain plane, in addition to a sufficiently small area of the front of each tube which can be approximated to a planar surface parallel to the strain plane (Fig. 2(b)). For accurate strain calculations on the curved area, the density of speckled surface should be sufficiently high in order to reduce plane approximation errors. After coordinate transformations, the data extracted from the image correlation system (VIC-3D) was checked against string pot measurements, and the results showed a satisfactory correlation (Fig. 2(c)). The error was less than 5% in most of the cycles in all test cases except at few points under maximum applied drift in the last cycle where severe local deformations occur, reaching a maximum of 10%. Strain gauges were also attached at specific points of the specimen for backup strain measurements in case of VIC-3D failure. The strain calculation procedure in VIC-3D is done considering the actual displacement vector (u, v, w) forming triangular

elements on the speckled surface. By validating the displacement vectors the strain values are accordingly verified.

3. Unilateral experimental results

Hysteresis curves for specimens tested under unilateral cyclic loading along with the backbone curve of the lateral pushover test conducted on the equivalent fabricated box section are shown in Fig. 3. As mentioned above, each specimen was subjected to an axial force equal to 25% of the member's compressive strength. The magnitudes of the axial forces applied on the specimens are compared in Table 2. By increasing the strength of tubes in fabricated sections, the overall strength and proportionally the applied axial force are increased (Javidan *et al*. 2016a). This increase is three times greater in the UHSS-C-1D specimen compared to the MS-C-1D specimen. The lateral strength cap increases with the rise in tube material. Compared to the backbone curve of the equivalent box, lateral strength and ductility improve as a result of the section geometry and the material of tube elements. Although the ductility of HSS and UHSS tube materials is individually lower than that of MS, the section geometry results in the interaction of plate and tube elements, which improves the overall ductility and lateral deformation capacity of sections by around 1.5 times. A slight pinching mechanism is observed in the lateral load-displacement curves of all three specimens initiating at displacement ratios higher than the cap strength. This phenomenon is due to the local buckling which occurs in MS plates under compression stresses
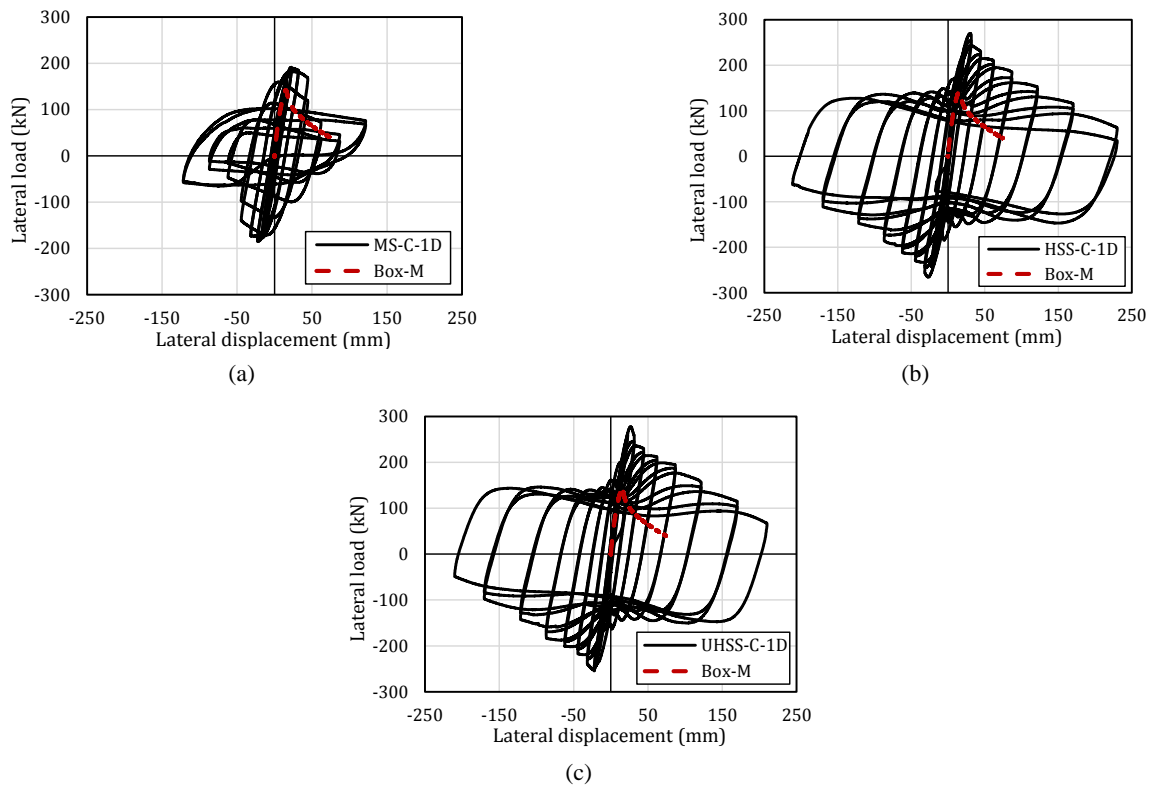

(a)

(b)

(c)

Fig. 3 Unilateral hysteresis curves a) MS-C-1D; b) HSS-C-1D and c) UHSS-C-1D.

Table 2 Main hysteresis properties of unilateral cyclic tests

	Box-M	MS-C-1D	HSS-C-1D	UHSS-C-1D
Axial compression capacity (kN)	660	1411	2836	4126
Applied axial force (kN)	165	353	709	1031
Lateral strength cap F_c (kN)	142	191	270	278

generated by the applied lateral shear forces. Hysteresis properties obtained from unilateral tests show that the incorporation of HSS and UHSS tubes enhances the lateral strength cap, while the section with stronger tube material undergoes a higher gravity load. However, the increase in lateral load-bearing capacity and the rise in tube strength properties do not show a linear relationship in the tested specimens. This nonlinearity is understood to be due to the relation between the strength and geometry of plate and tube elements. This will be explained in more detail in Section 3.2.

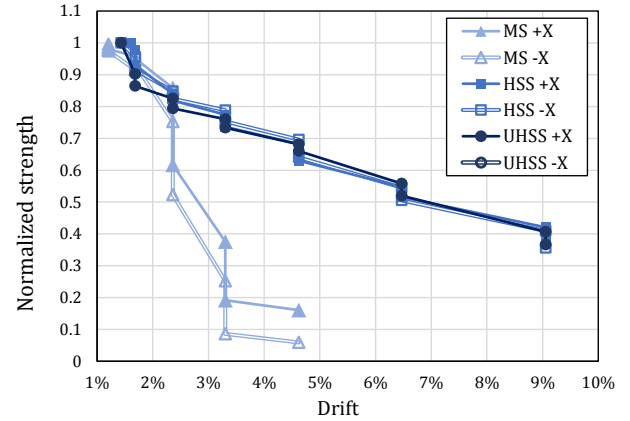### 3.1 Strength and stiffness degradation

3.1.1 Experimental observations

Normalized strength reductions of three specimens which initiates after certain number of cycles are compared in two positive and negative loading directions, and the results are presented in Fig. 4(a). Drift is defined as the ratio of the lateral displacement applied to the top of each tested column to the total effective column length. The lateral strength of each individual member is normalized relative to the hysteresis strength cap of that member presented in Table 2. Strength reduction was first observed after the 16th cycle in MS (corresponding to around 1.2% drift) and after the 18th cycle for HSS and UHSS sections (corresponding to around 1.6% and 1.5% drifts, respectively). This shows that increasing the tube strength can postpone the displacement corresponding to strength degradation initiation. Post peak strength reduction is similar in both HSS and UHSS specimens; however, a significantly sharper strength reduction is observed in MS member. For instance, at a specific drift of 3.3%, the lateral strength of column consisting of MS tubes is less than half of the full capacity, whereas for the two high-strength sections around 80% of full lateral strength is preserved.
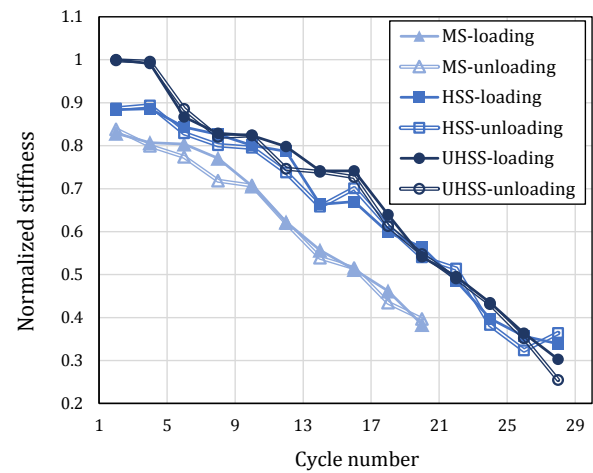
Fig. 4(b) shows the stiffness values for each specimen normalized to the initial stiffness of UHSS specimen. Since the stiffness of each cycle amplitude repeat is almost similar, the second repetition of each amplitude is presented. From the measurements it is evident that initial stiffness reduces with the decrease in tube strength, which is due to the higher lateral capacity of UHSS member compared to HSS and that compared to MS member. All member types show quite a similar stiffness degradation rate as cyclic loading progresses.

3.1.2 Calibration of the hysteretic deterioration model

With the aim of quantitative evaluation of post-capping strength and stiffness reduction of hybrid specimens, a deterioration model based on hysteretic energy dissipation
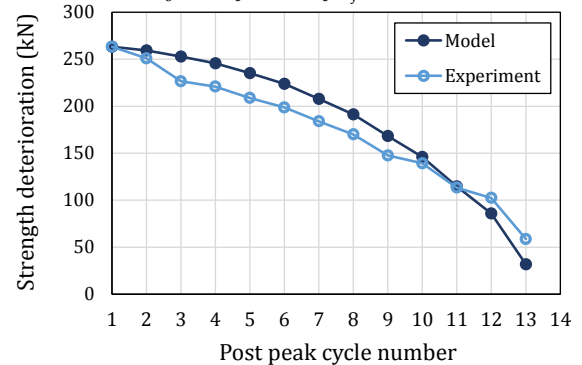

(a)

(b)

HSS-C-1D calibration of deterioration model parameters:
F_y=208 kN, δ_y= 16mm
α_s=0.2, α_c=-0.06, δ_c/δ_y=1.95, γ_s=210

(c)

Fig. 4 (a) Strength deterioration; (b) Stiffness deterioration in MS-C-1D, HSS-C-1D and UHSS-C-1D specimens; (c) Strength deterioration of HSS-C-1D member from model versus experiment along with calibrated parameters

is used (Ibarra 2003, Ibarra *et al.* 2005). This model assumes the hysteretic energy dissipation is independent of loading history (Rahnama and Krawinkler 1993). Knowing the actual energy dissipation capacity of hybrid members subjected to cyclic loading, the deteriorations parameters can be calibrated. Some initial parameters are obtained from the monotonic lateral load versus displacement backbone curve of each member. These parameters include F_y which is the yield strength; δ_y and δ_c which are the deformations corresponding to yield and capping (peak) points respectively; K_e, K_s ($= \alpha_s K_e$) and K_c ($= \alpha_c K_e$) which are the elastic, strain hardening and post-capping stiffness respectively. With regards to the hysteretic performance, a parameter called β_i is introduced in this model (Ibarra 2003) which defines the cyclic deterioration at cycle number i, based on the hysteretic energy dissipation of that cycle number, E_i, and the hysteretic energy dissipation capacity, E_t, as shown in Eq. (2).

$$\beta_i = \left(\frac{E_i}{E_t - \sum_{j=1}^{i} E_j} \right)^c \tag{2}$$

Parameter c defines the strength or stiffness deterioration rate. This value is calibrated with regards to the cyclic experimental data, thus β_i is obtained for each deterioration function. From the above-mentioned parameters, the strength and stiffness deterioration functions are derived based on the following equations

$$F_i = (1 - \beta_i)F_{i-1} \tag{3}$$

$$K_i = (1 - \beta_i)K_{i-1} \tag{4}$$

Fig. 4(c) illustrates the obtained strength deterioration model compared to the experiments along with presenting the calibrated model parameters for hybrid member consisting of HSS tubes. Due to a quite similar cyclic performance of both HSS-C-1D and UHSS-C-2D specimens, all calculations are conducted for the former member. Moreover, due to the similar performance of hybrid members in loading and unloading, the strain hardening slope is considered similar in both directions. Parameter γ expresses E_t as a function of twice the strain energy at yielding ($F_y \, \delta_y$). Comparing the calibrated monotonic backbone parameters of hybrid columns composed of HSS tubes to those of steel specimens previously reported in literature (Ibarra *et al.* 2005) shows a significantly higher strain hardening rate (α_c), a higher post-peak softening rate and a lower capping point to yield displacement ratio for the hybrid specimen. Regarding the hysteretic model parameters, γ value obtained for the hybrid specimen is higher than that of the steel specimen tested under standard loading protocols previously reported in literature (Ibarra *et al.* 2005). These differences imply the higher hysteretic energy dissipation capacity of the hybrid member. Parameter c was obtained equal to 1 for strength deterioration and equal to 1.1 for stiffness deterioration. The low value of c in these cases shows that the rate of strength and stiffness deterioration is fairly constant in the hybrid member.

3.2 Deformations and plastic hinge formation

A major effect of the tube material on the behavior of fabricated sections is in the plastic deformations along each strain generated in the tube elements of all hybrid specimens, the longitudinal direction is equivalent to the principle axes which is taken into consideration for the following plastic strain analysis. Strain measurements are plotted for 5 instances throughout the loading procedure, which sufficiently represent the general progress of cyclic test until failure. These measurement intervals are from the end of second repeat of cycles with drift percentages of 0.1%, 0.4%, 1.7%, 4.6% and 9%. For the MS-C-1D specimen, the ultimate applied drift was 6.5 so the graphs are plotted up to this point. With the aim of interpreting the magnitude of strain at different stages, values of yield and/or ultimate strain in each graph are also plotted with dashed lines. The maximum value of longitudinal strain in the MS-C-1D specimen reaches a significantly higher value (close to the ultimate strain of material (23%)) compared to that of the two other members (the peak strain hardly reaches 2%). The excessive strain values generated in the plates incorporated in the MS-C-1D specimen are due to the different failure mechanism and extreme axial shortening occurred in this member, which is understood to be a result of the distinct material properties of MS tube. The distinct behavior of the MS-C-1D member is also noticeable from the strain measurements of tube centerlines (Figs. 5(d)-(f)). MS tube reaches strain values up to 12% (i.e., higher than the strain corresponding to ultimate strength of MS tube material) at a final drift of 6.5%, while the ultimate strain values achieved by HSS and UHSS specimens remain less than the tube ultimate strain. The observation that strain values exceed the ultimate strain can also explain the higher rate of degradation in MS-C-1D specimen compared to the others. This indicates that high grades of steel in the members postpone material failure along beam-column elements preventing high rates of strength degradation and delaying overall failure.

These strain observations, show the effect of combined geometry and material of plates and tubes on the failure mechanism. In specimens with high strength tubes, throughout the entire loading process strain values in plates progress from yield to ultimate strain due to the high ductility of the plate material (i.e., high ultimate to yield strain ratio) while tubes remain below the ultimate strain at the column complete failure point. This interactive performance takes advantage of the high ductility of plates and the high strength of tubes. Accordingly, the overall mechanism of these specimens is governed by the ductile failure of plates while preventing sudden brittle fracture of the high strength tubes (i.e., low ultimate to yield strain ratio). The design of UHSS-C-1D, however, can be improved by increasing the width to thickness ratio of plates to increase the strain value of UHSS tube closer to the ultimate strain capacity of tube.

The distribution of plastic strain along the column is also worth comparison. In all tested specimens the strain is distributed along the entire length of the plate elements while in tube elements, plastic deformation is localized at the lower end in MS-C-1D and more towards the mid-
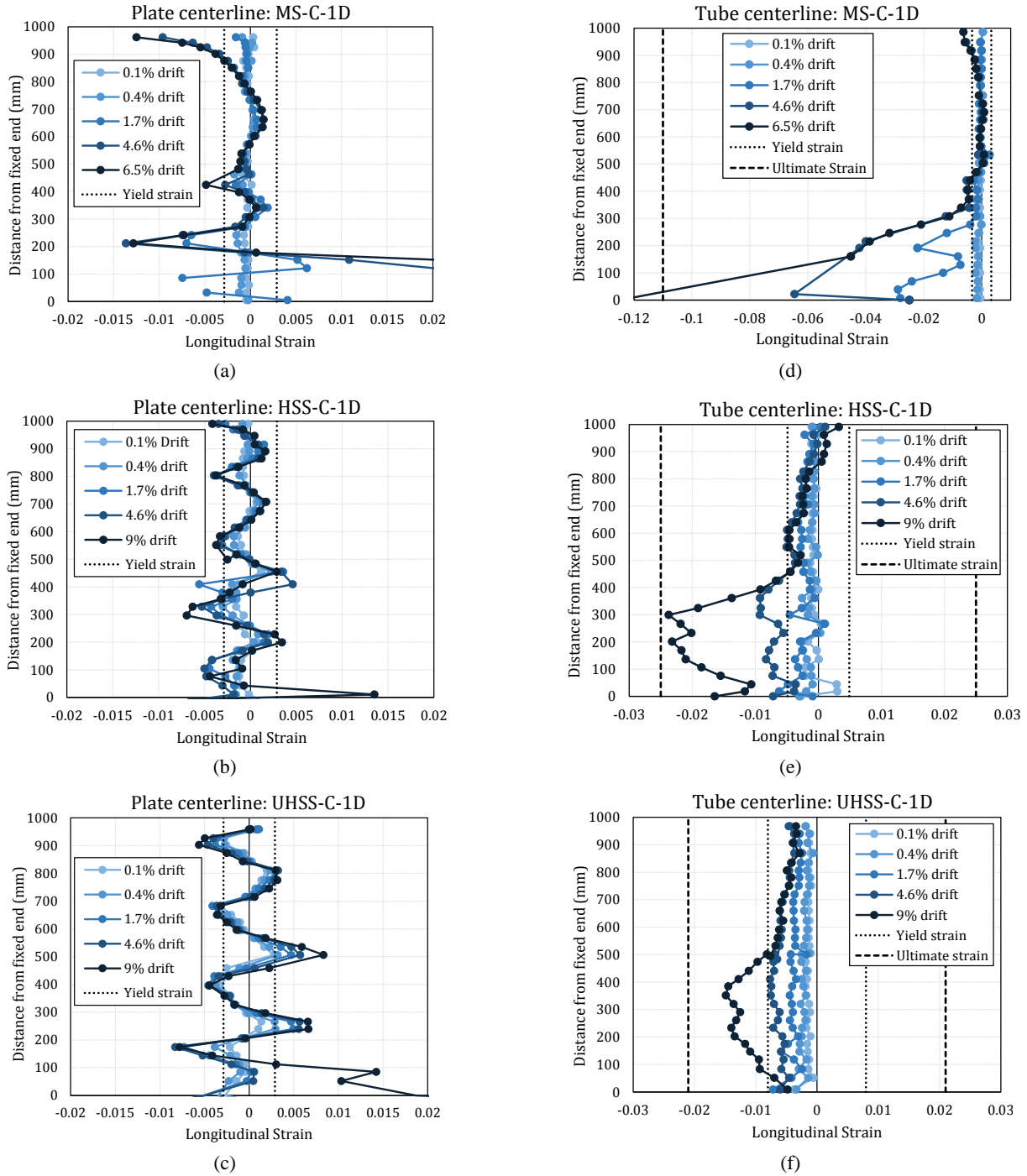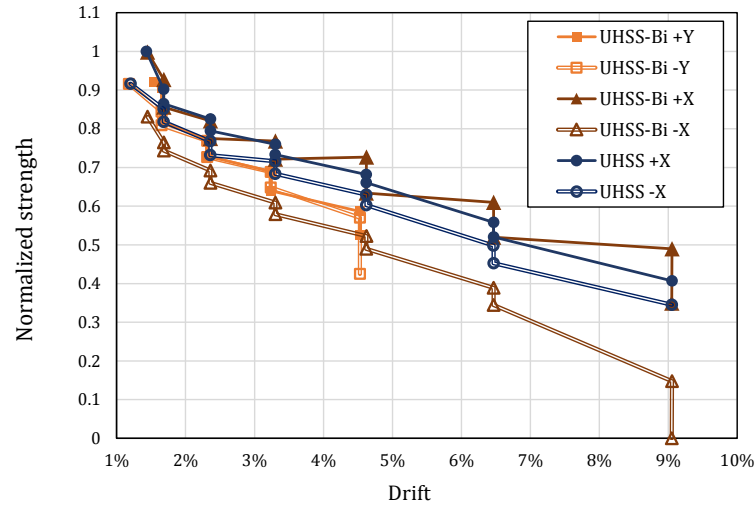
Fig. 5 Longitudinal strain distribution along plate centreline: (a) MS-C-1D; (b) HSS-C-1D; (c) UHSS-C-1D and tube centreline: (d) MS-C-1D; (e) HSS-C-1D; (f) UHSS-C-1D

length in HSS-C-1D and UHSS-C-1D. The width of the region on tube centerline with strain values higher than yield strain can be considered as the plastic hinge length. This length varies for different drift levels, depending on the value of cyclic amplitude and the steel tube material. The *plastic hinge ratio* is proposed for evaluating the plastic behavior and is defined as the ratio of the overall length of beam-column where longitudinal strain values exceed the material's yield strain to the total effective length of the element. In this study, since the plastic hinge length is measured at the bottom half of specimens, the plastic
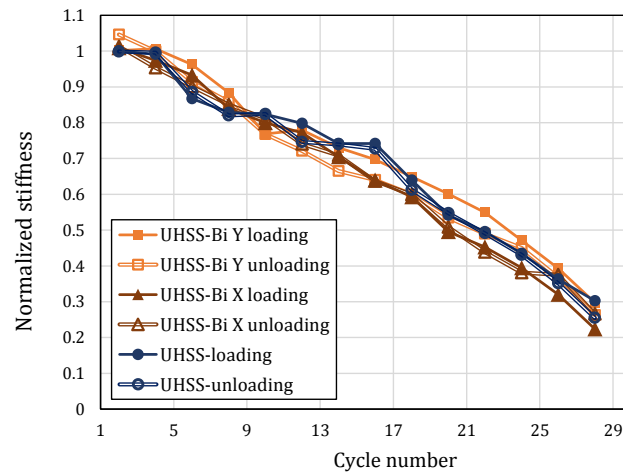
lengths are divided by half of the effective length (940mm). Plastic hinge ratios of tubes presented in Fig. 7(a) for three fabricated specimens are obtained for drift levels starting from the drift corresponding to strength cap up until ultimate failure. The plastic hinge length of UHSS-C-1D is equal to zero at the drift corresponding to strength cap meaning that the tube behavior is elastic and only approximately equal to 10% in the HSS-C-1D specimen. By progressing the applied lateral displacement to 4.5% drift, the hinge length tends to increase in all members. At a drift level of 6.5%, which is the final loading stage applied to

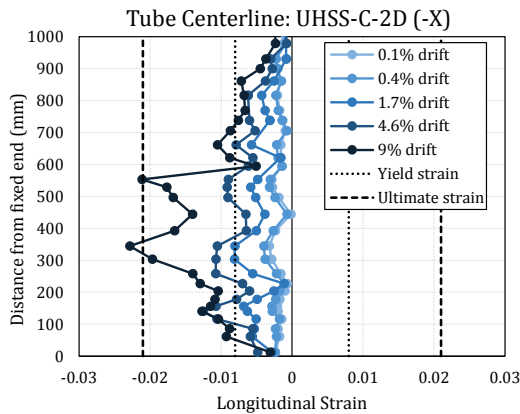Table 3 Main hysteresis properties of uniaxial and multiaxial cyclic tests

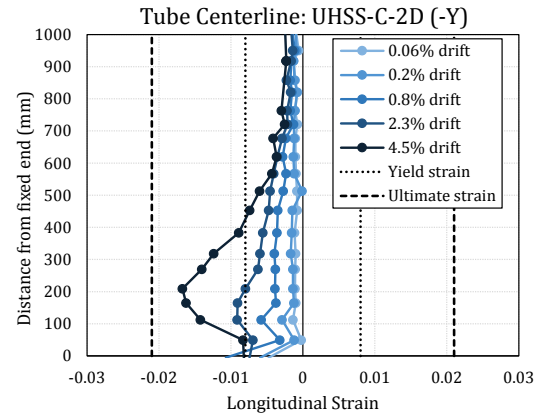|	UHSS-C-2D (+X)	UHSS-C-2D (-X)	UHSS-C-1D
Axial compression capacity (kN)	4126	4126	4126
Applied axial force (kN)	618	1444	1031
Lateral strength cap F_c (kN)	277	255	278

(a)

(b)

(c)

(d)

Fig. 6 Multiaxial cyclic tests: (a) Strength degradation; (b) stiffness degradation compared to uniaxial cyclic tests; longitudinal strain distribution along tube UHSS-C-2D centreline; (c) −X direction; (d) −Y direction

MS-C-1D, the plastic hinge length slightly reduces meaning that failure is localized at the lower end of the column where excessive plastic axial deformations take place. For HSS-C-1D tube plastic hinge length stabilizes with increasing cycle number, whereas that of UHSS-C-1D continues to increase up to the final cycle.

4. Bilateral experimental results

Multiaxial cyclic tests were conducted to account for the effect of the vertical component of earthquake forces and the overturning effects generated in external columns of structures subjected to earthquake. To understand the effect of cyclic axial and lateral loading on the mechanical performance and failure of high strength fabricated steel beam-columns, comparisons are drawn among experimental results of uniaxial and multiaxial tests (i.e., UHSS-C-1D and UHSS-C-2D), patterns shown in Fig. 1. The strength in the +X direction which undergoes less axial loading reaches higher values of lateral strength force compared to that of the −X direction and the strength degradation initiates at higher lateral displacement amplitude compared to that in the X direction (see Table 3).

4.1 Strength and stiffness degradation

In this section, the results of multiaxial cyclic loading are discussed and compared to those of uniaxial. Fig. 6(a) shows the strength degradation trend of the four lateral displacement directions (+X, -X, +Y and −Y) of the UHSS specimen against that of similar member under unilateral cyclic loading versus the drift values of each direction. In the Y direction, displacement amplitudes at each cycle are half of those applied in the X direction and the strength reduction in Y direction initiates at a greater number of cycles. Similar strength degradation trend is observed in +Y and −Y directions in which similar axial load is applied. The column cyclically loaded in the +X direction is subjected to an axial load which is 20% less than that in the -X direction, and this difference is evident in the normalized strength degradation curves showing the lowest lateral strength. At the end of cycle number 28 with the equivalent drift of 9% in −X direction, the member is unable to maintain the gravity loads in the presence of the applied lateral displacements which is the point of collapse. Stiffness degradation follows quite a similar trend despite the differences in axial load and amplitude (Fig. 6(b)).

4.2 Deformations and plastic hinge formation

Similar to the investigations reported in Section 3.1.2, variations in longitudinal strain values were captured at various stages of cyclic loading and the plastic deformations were analyzed. The longitudinal plastic strain along the beam-column under multiaxial cyclic loading in both -X and -Y directions are illustrated in comparison with steel material yield and ultimate strains (Figs. 6(c)-(d)). Note that in the -X direction 35% of axial compressive force is applied on the column while in the −Y direction 25% is applied. In the cycle with 1.7% drift, UHSS tube exceeds
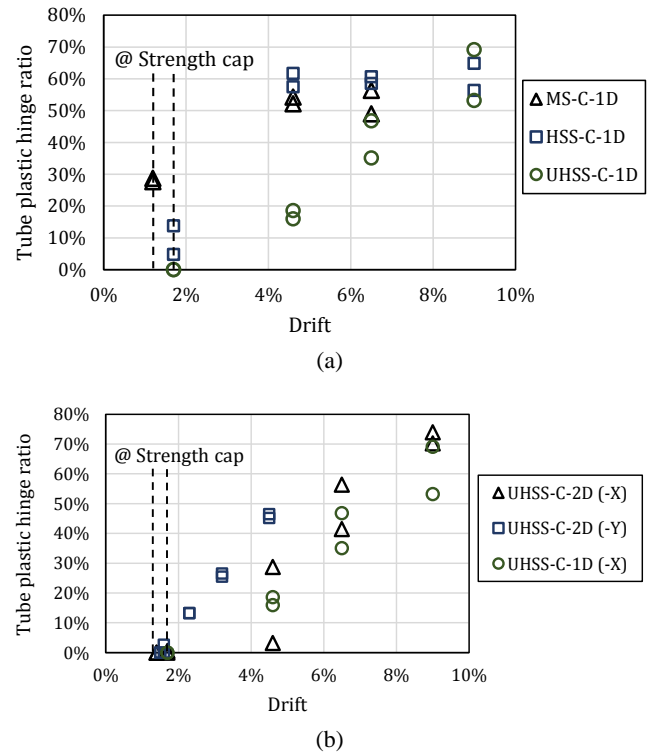

(a)

(b)

Fig. 7 Plastic hinge ratio of tube centrelines in:
(a) unilateral; (b) bilateral tests

yield strain level in the X direction and from that point onward strain levels increase with the increasing number of cycles applied. By the end of the final cycle (9% drift) some parts of the UHSS tube exceed the material ultimate strain, which is the point of complete collapse. The material's yield strain level are exceeded after applying drift levels of 0.8% in Y direction but remain below the ultimate strain by end of testing (28th cycle). The plastic hinge ratio was also obtained for both X and Y directions in the bilateral tests and compared with those for the unilateral UHSS-C-1D test (Fig. 7(b)). In both test cases, all tube elements remain elastic until the strength cap. In the −X direction with higher axial loads applied, the length of the plastic hinge ratio is higher than that in the unilateral test. The plastic hinge ratios of the two tube elements differ, due to the asymmetric application of axial forces in different directions. The specimen in −Y direction undergoes less drift compared to the −X direction, however, as a consequence of the replicated displacement cyclic history applied to the specimen, plastic hinge ratio increases with a higher slope and reaches amounts more than two times than the unilateral specimen when subjected to similar drift values.

5. Effect of axial force on the lateral performance of hybrid members

The variety of axial forces applied on hybrid high capacity members throughout the multiaxial cyclic protocols affect trend of strength deteriorations. The results of experimental tests showed a direct effect of axial load magnitude on the performance of hybrid beam-columns
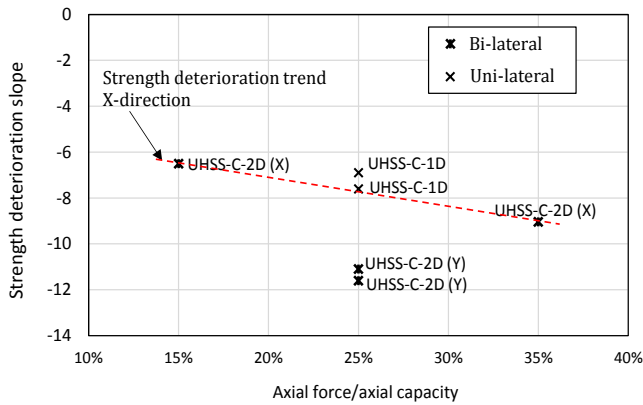
Fig. 8 Strength deterioration slope of UHSS-C-1D and UHSS-C-2D specimens versus applied axial force ratio

under unilateral and bilateral cyclic loading. To quantify these effects, strength deterioration was measured from the value of the slope of the normalized strength versus drift curve for each specimen and the results are presented in Fig. 8. *Strength deterioration slope* is defined as the slope of normalized strength deterioration versus the applied lateral drift at peak amplitude in a given direction. These negative slope values are extracted from both bilateral and unilateral tests conducted on specimens consisting of UHSS tubes which were subjected to a variety of axial load ratios in different directions. Strength deterioration slopes plotted as a function of the axial compression load ratio are illustrated in Fig. 8. The horizontal axis represents the ratio of axial force to the axial capacity of the member. The strength deterioration slope is shown to follow a linear decreasing trend for lateral X direction subjected to similar drift magnitudes. The strength deterioration slope in Y direction is more significant than that in the X direction, although the applied displacement amplitudes are half those in the X direction. At strength deterioration initiation in Y direction, the number of cycles undergone by the specimen is 22 compared to 18 cycles experienced with strength deterioration initiation in X direction. Therefore, the greater number of cycles in addition to the effect of cycle damage from the X direction displacement history, results in a more significant strength deterioration slope in this direction. Due to the fact that only one direction of lateral cyclic load was applied to UHSS-C-1D specimen, the strength deterioration slope for this specimen is slightly less than that of the multiaxial test. Strength deterioration slop obtained in this section has a direct relationship with the post-capping stiffnness in the hysteretic deterioration model (Ibarra 2003), $K_c (= \alpha_c K_e)$, due to similar elastic stiffness values for all cases. This shows that variation in the parameter α_c will also follow a linear tend as a function of the applied axial force.

6. Failure mechanism and axial shortening

In addition to the overall strength, displacements and plastic behavior, changing the tube material also affects the

failure mechanism of each specimen. The deformed shapes of each hybrid member under uniaxial and multiaxial cyclic loadings are shown in Fig. 9. These images show each failed specimen under the application of final drift amplitude of cyclic test. In the first three images, effect of the steel tube material on the failure of hybrid fabricated components is clearly evident. With the application of cyclic lateral displacement on MS-C-1D specimen, the majority of local deformation occurs in areas close to the end of specimen in both plates and tubes. The type of deformation observed is the folding mechanism known to be an indication of ductile behavior (Zhao and Grzebieta 1999). This folding occurs at both ends of the hollow section which is similar to the results reported for other hollow circular steel sections (Zhao *et al*. 2010). However, due to the simultaneous effect of axial and lateral forces, inward folding is observed in the surface vertical to lateral cyclic direction (X) and outward folding in the direction parallel to lateral cycles at the top and bottom of specimen. However, in HSS-C-1D and UHSS-C-1D, local lateral shear deformation occurs along the total length of MS plates which is due to the compression forces generated throughout the width of plates on the side parallel to lateral displacement direction. Because of the higher ductility of MS tubes compared to that of high strength steel tubes, MS-C-1D undergoes severe local deformations at both ends under the applied axial and lateral displacements. In contrast, the HSS and UHSS tubes show global deformation curvature along the members. In the UHSS-C-2D specimen plate deformations occur in two directions and the most severe deflections are formed in the X direction compared to that of Y direction and also compared to the unilateral specimens. In addition to the differences in plate and tube mechanisms, the bilateral displacement applied to the UHSS-C-2D specimen with asymmetric axial loads affects the overall squareness of the section geometry at failure.

When a steel frame is subjected to earthquake excitation, column elements undergo axial deformations. This shortening is a result of the longitudinal strains generated from the combined action of axial loads, coming from the constant effect of gravity load and the vertical component of earthquake load, as well as the cumulative longitudinal strains of bending moments developed from reversed lateral displacements. Depending on the direction of lateral loads bending moments cause compressive strains at either side of the neutral axis which result in a gradual axial shortening (MacRae *et al*. 2009). The axial deformation in Z direction is obtained from the testing machine crosshead reading and because the LVDT measurements showed no deformation in the concrete pedestal and the top steel plates relative to the crosshead, this value actually demonstrates the axial displacement at the top of each specimen. Axial displacements are plotted for four specimens tested under unilateral and bilateral cyclic loads shown below the failure mechanisms in Fig. 9. These displacement measurements demonstrate the significant effect of tube material properties on the axial shortening of beam-column members subjected to lateral cyclic displacements. MS-C-1D (Fig. 9(a)) shows an axial shortening of around 15 times more than members
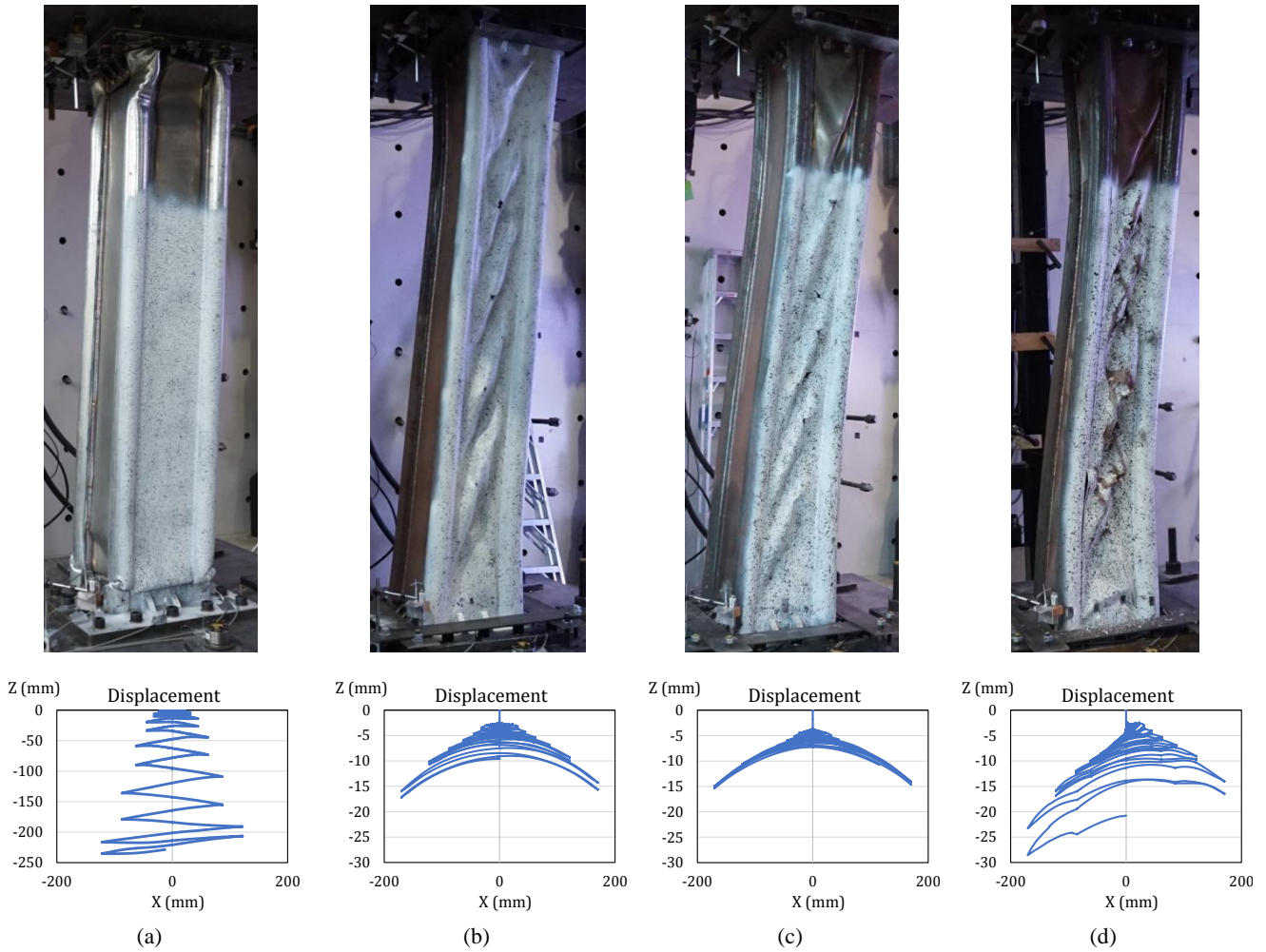
Fig. 9 Failure mechanism of fabricated members and axial displacement throughout the cyclic test in X direction for:
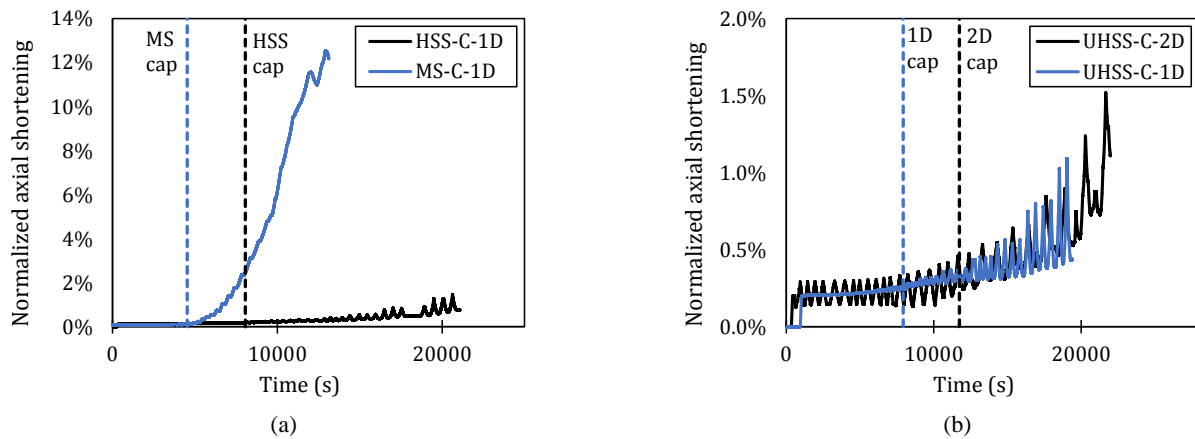(a) MS-C-1D; (b) HSS-C-1D; (c) UHSS-C-1D; and (d) UHSS-C-2D specimens

Fig. 10 Normalized axial shortening comparison among: (a) MS-C-1D and HSS-C-1D; and (b) UHSS-C-1D and
UHSS-C-2D specimens

consisting of high strength tubes (Figs. 9(b), (c) and (d)). The asymmetric axial loading pattern applied on UHSS-C-2D specimen resulted in asymmetric axial displacements in two opposite directions. Detailed comparisons of the axial shortenings normalized by the effective length for the MS-C-1D and HSS-C-1D specimens are illustrated in Fig. 10. Axial deformation of MS-C-1D increases significantly after the specimen reaches its lateral strength cap, shown with dashed lines in Fig. 10(a). This is due to the ductile plastic behavior of MS tubes resulting in local buckling and

excessive local deformations during cyclic testing. This observation is similar in all other specimens which show that significant axial shortening initiates after exceeding the displacement corresponding to lateral strength cap. The effect of multiaxial loading can be observed by comparing UHSS-C-1D and UHSS-C-2D curves in Fig. 10(b). By comparing the bilateral axial shortening measurements with the unilateral test case, in which the magnitude of axial force is the mean value of that in the bilateral test, it can be concluded that lower axial force results in less shortening in specimens. However, this trend is observed before reaching the strength cap. After exceeding the drift corresponding to strength cap, axial shortening of UHSS-C-2D in the direction with less axial compression force starts to increase relative to the unilateral test. This is because in bilateral tests, moments in the X direction result in axial compressive strains in half of the section, which accumulate with the compressive strains generated from the moments occurring during lateral displacements in Y direction. The change in length of a column Δ_a was also obtained for HSS-C-1D and UHSS-C-1D specimens as a function of the cumulative inelastic rotation $\sum \theta_H = \sum \mu_H \, \delta_p / L_c$, where $\sum \mu_H$ is the cumulative inelastic ductility, δ_p is the displacement at the top of the beam-column and L_c is the total length (MacRae *et al.* 2006). The results show that shortening versus accumulative inelastic rotation follows a trend which approximates a bilinear curve with different slopes before and after the cycle corresponding to the cap lateral strength. The accumulative inelastic rotation at strength cap was 0.17 for HSS-C-1D and 0.19 for UHSS-C-1D at the end of the 18th cycle when 1.7% drift was applied.

7. Conclusions

Hysteresis characteristics obtained from unilateral tests on fabricated hybrid sections showed that the incorporation of high and ultra-high strength tubes enhances the lateral strength cap compared to the section with mild tubes by more than 2 times. In the section with MS tubes at 3.3% drift, a sharp strength reduction of more than 50% was observed, whereas in the two high strength sections under the same drift, 80% of strength was preserved. This indicates that high grades of steel material in the members postpones material failure along the beam-column elements preventing high rates of strength degradation and delaying overall failure.

Using the well-known hysteretic Ibarra model, deterioration parameters of hybrid specimens were calibrated against the experimental results and compared to those of conventional steel specimens. These parameters imply the higher hysteretic energy dissipation capacity of the hybrid member. The obtained model can be used to accurately assess and predict the seismic response of structures consisting of these types of high capacity components from the onset of damage through to collapse.

Plastic strain measurements along members tested under unilateral and bilateral cyclic amplitudes showed that mild steel plates undergo greater amounts of plastic deformation distributed along the specimen length. Longitudinal strains exceed yield values just after the drift corresponding to strength cap (10% plastic hinge ratio) in specimen with HSS tubes and remains fully elastic (0% plastic hinge ratio) in the specimen with UHSS tubes. Based on the observed dual action of the two different steel elements, strain values in plates progress from yield to ultimate strain due to their high ductile nature (i.e., high ultimate to yield strain ratio). In this interactive performance, the overall mechanism of these specimens are governed by the ductile failure of plates rather than the sudden brittle fracture of the high strength tubes (due to their low ultimate to yield strain ratio) taking advantage of the high ductility of plates and the high strength of tubes.

The strength data extracted from unilateral and bilateral tests showed that the lateral strength deterioration slope and therefore the post-capping stiffness of hybrid specimens follow a linear decreasing trend as a function of the applied axial force in specimens subjected to similar drift magnitudes. Finally, studying the axial deformation of tested specimens indicates that incorporating high strength steel tubes reduces the axial shortening of specimens more than 15 times which prevents undesirable effects such as excessive deformations especially in the base of a frame.

References

Amadio, C., Bedon, C., Fasan, M. and Pecce, M.R. (2017), "Refined numerical modelling for the structural assessment of steel-concrete composite beam-to-column joints under seismic loads", *Eng. Struct.*, **138**, 394-409.

Amraei, M., Skriko, T., Björk, T. and Zhao, X.-L. (2016), "Plastic strain characteristics of butt-welded ultra-high strength steel (UHSS)", *Thin-Wall. Struct.*, **109**, 227-241.

Aoki, T. and Susantha, K.A.S. (2005), "Seismic performance of rectangular-shaped steel piers under cyclic loading", *J. Struct. Eng.*, **131**(2), 240-249.

Azhari, F., Heidarpour, A., Zhao, X.L. and Hutchinson, C.R. (2017), "Effect of creep strain on mechanical behaviour of ultra-high strength (Grade 1200) steel subject to cooling phase of a fire", *Constr. Build. Mater.*, **136**, 18-30.

Banfi, M.J.A., Cardwell, S., Gedge, G. and Murgatroyd, E.C. (2005), "Material and workmanship requirements for modern codes of practice", *Steel Compos. Struct., Int. J.*, **5**(2), 169-180.

Bousias, S.N., Verzeletti, G., Fardis, M.N. and Gutierrez, E. (1995), "Load-path effects in column biaxial bending with axial force", *J. Eng. Mech.*, **121**(5), 596-605.

Dubina, D., Stratan, A., Vulcu, C. and Ciutina, A. (2014), "High strength steel in seismic resistant building frames", *Steel Constr.*, **7**(3), 173-177.

ElMandooh Galal, K. and Ghobarah, A. (2003), "Flexural and shear hysteretic behaviour of reinforced concrete columns with variable axial load", *Eng. Struct.*, **25**(11), 1353-1367.

Fadden, M. and McCormick, J. (2012), "Cyclic quasi-static testing of hollow structural section beam members", *J. Struct. Eng.*,

138(5), 561-570.

Farahi, M. and Erfani, S. (2017), "Employing a fiber-based finite-length plastic hinge model for representing the cyclic and seismic behaviour of hollow steel columns", *Steel Compos. Struct., Int. J.*, **23**(5), 501-516.

Farahi, M., Heidarpour, A., Zhao, X.-L. and Al-Mahaidi, R. (2017), "Effect of ultra-high strength steel on mitigation of non-ductile yielding of concrete-filled double-skin columns", *Constr. Build. Mater.*, **147**, 736-749.

FEMA461 (2007), Interim testing protocols for determining the seismic performance characteristics of structural and nonstructural components; Applied Technology Council, CA, USA.

Fogarty, J. and El-Tawil, S. (2016), "Collapse resistance of steel columns under combined axial and lateral loading", *J. Struct. Eng.*, **142**(1), 04015091.

Girão Coelho, A.M. and Bijlaard, F.S.K. (2010), "Finite element evaluation of the strength behaviour of high-strength steel column web in transverse compression", *Steel Compos. Struct., Int. J.*, **10**(5), 385-414.

Goto, Y., Jiang, K. and Obata, M. (2006), "Stability and ductility of thin-walled circular steel columns under cyclic bidirectional loading", *J. Struct. Eng.*, **132**(10), 1621-1631.

Hashemi, M.J., Al-Mahaidi, R., Kalfat, R. and Burnett, G. (2014). "State-of-the-Art System for Hybrid Simulation at Swinburne", *Australian Earthquake Engineering Society Conference 2014*, Lorne, Australia, November.

Heidarpour, A., Cevro, S., Song, Q.Y. and Zhao, X.L. (2014), "Behaviour of stub columns utilising mild-steel plates and VHS tubes under fire", *J. Constr. Steel Res.*, **95**, 220-229.

Hosseini, S., Heidarpour, A., Collins, F. and Hutchinson, C.R. (2016), "Strain ageing effect on the temperature dependent mechanical properties of partially damaged structural mild-steel induced by high strain rate loading", *Constr. Build. Mater.*, **123**, 454-463.

Ibarra, L.F. (2003), *Global Collapse of Frame Structures under Seismic Excitations*, Stanford University.

Ibarra, L.F., Medina, R.A. and Krawinkler, H. (2005), "Hysteretic models that incorporate strength and stiffness deterioration", *Earthq. Eng. Struct. Dyn.*, **34**(12), 1489-1511.

Javidan, F., Heidarpour, A., Zhao, X.L. and Minkkinen, J. (2015a), "Compressive behavior of innovative hollow long fabricated columns utilizing high strength and ultra-high strength tubes", *Tubular Structures - Proceedings of the 15th International Symposium on Tubular Structures, ISTS 2015*.

Javidan, F., Heidarpour, A., Zhao, X.L. and Minkkinen, J. (2015b), "Performance of innovative fabricated long hollow columns under axial compression", *J. Constr. Steel Res.*, **106**, 99-109.

Javidan, F., Heidarpour, A., Zhao, X.-L. and Minkkinen, J. (2016a), "Application of high strength and ultra-high strength steel tubes in long hybrid compressive members: Experimental and numerical investigation", *Thin-Wall. Struct.*, **102**, 273-285.

Javidan, F., Heidarpour, A., Zhao, X.-L., Hutchinson, C.R. and Minkkinen, J. (2016b), "Effect of weld on the mechanical properties of high strength and ultra-high strength steel tubes in fabricated hybrid sections", *Eng. Struct.*, **118**, 16-27.

Javidan, F., Heidarpour, A., Zhao, X.-L. and Al-Mahaidi, R. (2017), "Bending moment and axial compression interaction of high capacity hybrid fabricated members", *Thin-Wall. Struct.*, **121**, 89-99.

Kulkarni, N.G., Kasai, A. and Tsuboi, H. (2009), "Displacement based seismic verification method for thin-walled circular steel columns subjected to bi-directional cyclic loading", *Eng. Struct.*, **31**(11), 2779-2786.

Lian, M., Su, M. and Guo, Y. (2015), "Seismic performance of eccentrically braced frames with high strength steel combination", *Steel Compos. Struct., Int. J.*, **18**(6), 1517-1539.

MacRae, G.A., Hyde, K., Walpole, W.R., Moss, P., Hyland, C., Clifton, C. and Mago, N. (2006), *Column Axial Shortening Effects in Steel Frames*.

MacRae, G.A., Urmson, C.R., Walpole, W.R., Moss, P., Hyde, K. and Clifton, C. (2009), "Axial shortening of steel columns in buildings subjected to earthquakes", *Bull. New Zealand Soc. Earthq. Eng.*, **42**(4), 275-287.

Mamaghani, I.H.P. (2010), "Seismic performance evaluation of steel tubular columns under cyclic bidirectional loading", *Tubular Structures XIII - Proceedings of the 13th International Symposium on Tubular Structures*.

Mirmomeni, M., Heidarpour, A., Zhao, X.-L., Hutchinson, C.R., Packer, J.A. and Wu, C. (2015), "Mechanical properties of partially damaged structural steel induced by high strain rate loading at elevated temperatures – An experimental investigation", *Int. J. Impact Eng.*, **76**, 178-188.

Nakashima, M. and Liu, D. (2005), "Instability and complete failure of steel columns subjected to cyclic loading", *J. Eng. Mech.*, **131**(6), 559-567.

Nassirnia, M., Heidarpour, A., Zhao, X.-L. and Minkkinen, J. (2015), "Innovative hollow corrugated columns: A fundamental study", *Eng. Struct.*, **94**, 43-53.

Park, J., Lee, J. and Kim, J. (2012), "Cyclic test of buckling restrained braces composed of square steel rods and steel tube", *Steel Compos. Struct., Int. J.*, **13**(5), 423-436.

Rahnama, M. and Krawinkler, H. (1993), *Effect of Soft Sooils and Hysteresis Models on Seismic Design Spectra*, Department of Civil Engineering, Stanford University.

Rodrigues, H., Furtado, A. and Arêde, A. (2016), "Behavior of rectangular reinforced-concrete columns under biaxial cyclic loading and variable axial loads", *J. Struct. Eng.*, **142**(1), 04015085. DOI: http://dx.doi.org/10.1061/(ASCE)ST.1943-541X.0001345

Sadeghi, S.N., Heidarpour, A., Zhao, X.-L. and Al-Mahaidi, R. (2017), "An innovative I-beam to hybrid fabricated column connection: Experimental investigation", *Eng. Struct.*, **148**, 907-923.

Sinaie, S., Heidarpour, A. and Zhao, X.L. (2016), "Effect of pre-induced cyclic damage on the mechanical properties of concrete exposed to elevated temperatures", *Constr. Build. Mater.*, **112**, 867-876.

Ucak, A. and Tsopelas, P. (2015), "Load path effects in circular steel columns under bidirectional lateral cyclic loading", *J. Struct. Eng.*, **141**(5), 04014133.
DOI: http://dx.doi.org/10.1061/(ASCE)ST.1943-541X.0001057

VIC-3D, Non-contacting Measurement Solutions; Correlated-Solutions.

Wang, Y.B., Li, G.Q., Cui, W. and Chen, S.W. (2014), "Seismic behavior of high strength steel welded beam-column members", *J. Constr. Steel Res.*, **102**, 245-255.

Wang, Y.B., Li, G.Q., Cui, W., Chen, S.W. and Sun, F.F. (2015), "Experimental investigation and modeling of cyclic behavior of high strength steel", *J. Constr. Steel Res.*, **104**, 37-48.

Ye, J.H., Zhao, X.L., Van Binh, D. and Al-Mahaidi, R. (2007), "Plastic mechanism analysis of fabricated square and triangular sections under axial compression", *Thin-Wall. Struct.*, **45**(2), 135-148.

Zhao, X.L. and Grzebieta, R. (1999), "Void-filled SHS beams subjected to large deformation cyclic bending", *J. Struct. Eng.*, **125**(9), 1020-1027. Zhao, X.L., Tong, L.W. and Wang, X.Y. (2010), "CFDST stub columns subjected to large deformation axial loading", *Eng. Struct.*, **32**(3), 692-703.

BU